Published in final edited form as:

J Am Chem Soc. 2018 October 10; 140(40): 12808–12818. doi:10.1021/jacs.8b05777.

Implications of Pyran Cyclization and Pterin Conformation on Oxidized Forms of the Molybdenum Cofactor

Douglas R. Gisewhite[a], **Jing Yang**[b], **Benjamin R. Williams**[a], **Alisha Esmail**[a], **Benjamin Stein**, **Martin L. Kirk**[b], and **Sharon J. N. Burgmayer**[a]

[a]Department of Chemistry, Bryn Mawr College, Bryn Mawr, Pennsylvania 19010, United States

[b]Department of Chemistry and Chemical Biology, The University of New Mexico, MSC03 2060, 1 University of New Mexico, Albuquerque, New Mexico 87131-0001, United States

Abstract

The large family of mononuclear molybdenum and tungsten enzymes all possess the special ligand molybdopterin (MPT), which consists of a metal-binding dithiolene chelate covalently bound to a pyranopterin group. MPT pyran cyclization/scission processes have been proposed to modulate the reactivity of the metal center during catalysis. We have designed several small molecule models for the Mo-MPT cofactor that allow detailed investigation into how pyran cyclization modulates electronic communication between the dithiolene and pterin moieties, and how this cyclization alters the electronic environment of the molybdenum catalytic site. Using a combination of cyclic voltammetry (CV), vibrational spectroscopy (FT-IR and rR), electronic absorption spectroscopy, and x-ray absorption spectroscopy (XAS), distinct changes in the Mo≡O stretching frequency, Mo(V/IV) reduction potential, and electronic structure across the pterin-dithiolene ligand are observed as a function of pyran ring closure. The results are significant for they reveal that a dihydropyranopterin is electronically coupled into the Mo-dithiolene group due to a coplanar conformation of the pterin and dithiolene units, providing a mechanism for the electron-deficient pterin to modulate the Mo environment. A spectroscopic signature identified for the pyranodihydropterin-dithiolene ligand on Mo is a strong dithioleneàpterin charge transfer transition. In the absence of a pyran group bridge between pterin and dithiolene, the pterin rotates out of plane, largely decoupling the system. The results support a hypothesis that pyran cyclization/scission processes in MPT may function as a molecular switch to electronically couple and decouple the pterin and dithiolene to adjust the redox properties in certain pyranopterin molybdenum enzymes.

TOC graphic.

corresponding author: sburgmay@brynmawr.edu.

Supporting Information.

ESI-MS, ^{1}H, and HSQC NMR data for **2**; UV-vis spectra of **1** and **2** in acetonitrile and $CHCl_3$; experimental and computed resonance Raman spectra for **1**; rR profiles for **2**; band assignments from electronic absorption spectroscopy and associated EDDMs for Bands A, C, and D in **1**; Mo K-edge XANES and FT of EXAFS for **1** and **2**. This material is available free of charge via the Internet at http://pubs.acs.org.

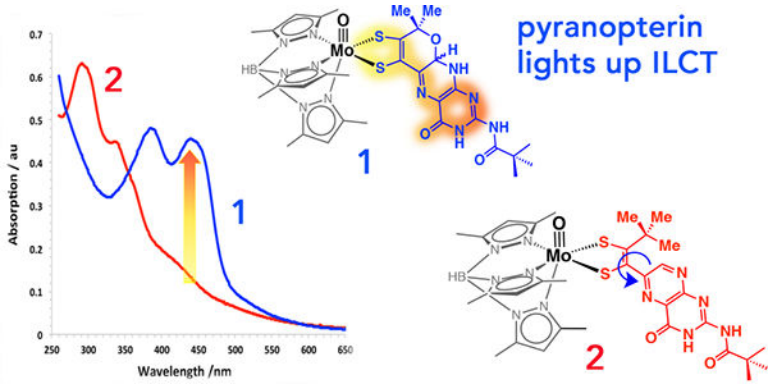

Keywords

Molybdenum enzymes; Moco; pyranopterin dithiolene; molybdopterin; intraligand charge transfer

Introduction

The catalytic center of molybdenum and tungsten enzymes consists of a Mo or W ion coordinated by one or two pyranopterin dithiolene ligands (Fig. 1).[1–5] The pterin-substituted dithiolene chelate is unique to a large group of more than fifty enzymes distributed through all phyla, and its structure has been largely conserved throughout evolution from the earliest bacteria over billions of years.[6] This ligand, originally named molybdopterin (MPT),[7] is ubiquitous throughout nature but remains an enigma because its role in catalysis is unknown. Protein crystal structures have provided hints of possible roles for MPT, including creating a hydrogen-bonded anchor for the metal (Mo or W), modulating the metal ion reduction potential, and serving as a conduit for electron transfer to FeS clusters hydrogen-bonded directly to the pterin.[8–16] Unfortunately, protein crystal structures do not reveal how the pterin dithiolene ligand tunes the electronic environment of the Mo or W ion to properly poise it for catalysis, nor do these static structures provide any information regarding dynamic changes of conformation or oxidation state at MPT. There is no spectroscopic data that might indicate how the pterin influences catalysis. Obtaining this critical information from spectroscopy is hampered by the presence of competing chromophores in the protein and the instability of the cofactor once removed from the protein matrix. While the majority of X-ray structures depict MPT as a fully reduced tetrahydropyranopterin, an analysis of 102 protein structures strongly supports the hypothesis that specific pyranopterin conformations are associated with a given canonical enzyme family, and that these conformations are related to their function.[17] This analysis of pyranopterin structures also concluded that within the DMSO reductase (DMSOR) family, the Mo ion is coordinated by two *different* MPT ligands.[17–18] Indeed, structures of nitrate reductase (NarGHI)[19], ethylbenzene dehydrogenase (EBDH)[20] and perchlorate reductase (PcrAB)[21] all exhibit the proximal MPT ligand in the typical bent tricyclic tetrahydropyranopterin structure (Fig. 1; red) whereas the distal MPT lacks the pyran ring and consists of a simple bicyclic pterin ring system (Fig. 1; blue). These structures of the catalytic site with differentiated pterins are strongly suggestive of specific functions for each individual pterin.[17] Furthermore, a role for

MPT in electron transfer would be facilitated by the extraordinary electronic flexibility of the redox active dithiolene and pterin units and may account for the remarkably diverse range of substrates within the DMSOR class of metalloenzymes.[4, 18] Several recent reports provide evidence for a direct MPT role in catalysis, citing the dependence of the Mo(V/IV) reduction potential on H-bonding interactions between amino acids and the B and C portions of MPT (Fig. 1),[22–23] and electrochemical evidence for a redox-active pyranopterin in the catalytic cycle of YedY.[24] Unfortunately, with *no direct experimental evidence* that defines the oxidation state of the pterin in the enzymes these possibilities remain speculative.

Thus, our approach to understanding the effects of pterin oxidation state, open-form and pyrano-form MPTs, and identifying the catalytic role of MPT within the molybdenum cofactor (Moco) is to investigate the chemistry of small molecule analogues containing specifically tailored pterin-dithiolene ligands. We recently demonstrated the usefulness of this analogue approach by describing a Mo complex of a pterin dithiolene (**1**) that exhibits a reversible pyranopterin cyclization (Fig. 2).[25] The equilibrium and thermodynamics of pyranopterin formation were studied for [TEA][Tp*Mo(O)(S_2BMOPP)][26] (**1**) as a function of the solvent dielectric.[27] In these studies, we observed pyran ring formation in **1** to be favored in polar solvents, whereas pyran ring scission occurs in low polarity solvents. These results suggest that the protein environment might exert control over reversible pyran ring cyclization during catalysis. Recent studies of nitrate reductase from both *E. coli* (NarGHI) and *Rhodobacter sphaeroides* (NapAB) proposed this pyran cyclization process as a step preceding a pre-reduction activation required for catalytic activity in heterogeneous samples.[28–29]

We have now synthesized a new model compound **2** (Fig. 2) and in this manuscript we make a direct comparison with Mo-pterin-dithiolene complex **1** in order to probe the consequences of pyran ring formation at the Mo center. Specifically, we evaluate the effects of the pterin π-system in the ring-opened configuration of **2**, which is expected to exhibit decreased electronic communication between pterin and dithiolene since the π systems of the dithiolene and pterin units become decoupled. The work is important not only for evaluating electronic structure differences between ring-opened and ring-closed pyran forms of the cofactor, but for understanding the spectroscopic signatures associated with this process. Due to the presence of other more highly absorbing chromophores in most of the enzymes, it has been impossible to obtain spectral data from MPT. Thus, the results we obtain from models **1** and **2** provide a basis for further understanding the role of the pyranopterin in fine-tuning the Mo redox potential to control catalytic activity in some molybdoenzymes.

Results and Analysis

Synthesis and Structure.

Preparation of **1** followed our general methodology[30] for synthesizing a variety of pterin dithiolene model complexes that has been previously reported.[25, 27] Since compound **1** exists in solution as an equilibrium mixture of both pyranopterin (**1_p**) and open pterin forms (**1_o**), it is not possible to use **1** for assessing the impact of pyran cyclization on the Mo electronic environment. To circumvent this problem, we designed a new complex, [TEA]

[Tp*Mo^{IV}(O)(S_2BDMPP)][26] (**2**) (Fig. 2, right), where isosteric replacement of the hydroxyl group in **1** with a methyl group precludes pyran ring formation.

The synthesis of **2** is shown in Scheme 1. Reaction of the pterinylalkyne, BDMPP, with [TEA][Tp*Mo(S)(S_4)] produces [TEA][Tp*Mo(S)(S_2BDMPP)] (**3)**. Hydrolysis of the Mo≡S group in **3** by adventitious water mediated by tri-*n*-butylphosphine in acetonitrile (ACN) produces the Mo≡O group in **2**. Characterization of the target complex **2** employed both ESI-MS and ^{1}H NMR (see Supporting Information) in order to confirm bulk sample structure and purity. Using FT-IR, cyclic voltammetry, electronic and resonance Raman spectroscopies to report variation at the Mo environment of **1** and **2**, we observe distinct changes in the Mo≡O stretching frequency, Mo(V/IV) reduction potential, and electronic structure within the pterin-dithiolene ligand, described in detail below.

The x-ray crystallographic structure of $\mathbf{1_p}$[25] is presented in Fig. 3 to illustrate how the pyran ring enforces a nearly coplanar arrangement of the dithiolene chelate and the pterin. Since the open form $\mathbf{1_o}$ was not observed crystallographically, DFT geometry optimizations revealed its most stable rotomer positions the pterin ~30° out of planity with the dithiolene chelate, a conformer stabilized by an intramolecular H-bond between the side chain hydroxyl and N5.[27] In the absence of an X-ray structure for **2**, DFT calculations were used to obtain an optimized structure (Fig. 3, right) that shows how the steric repulsion of the *t*-butyl group prevents coplanarity of the dithiolene chelate with the pterin, causing the pterin to rotate ~40° rotation away from the Mo-dithiolene plane. Thus, the pterin rotation relative to the Mo-dithiolene plane in the open form $\mathbf{1_o}$ is similar to that of **2**. Since the x-ray crystal structure of **2** has not been determined, we have used Mo K-edge x-ray absorption near edge structure (XANES) and extended x-ray absorption fine structure (EXAFS) data (Figures S7 and S16; Table S3) to probe the first coordination sphere similarity between **1** and **2**. The EXAFS data confirms the Mo(IV) oxidation state and first coordination sphere structural similarity between $\mathbf{1_p}$ and **2**.

Electrochemical Characterization.

The impact of pyran cyclization on the Mo(V/IV) redox couple has been measured by cyclic voltammetry. The reversible Mo(V/IV) redox processes shown in Fig. 4 for **1** (blue) and **2** (red) in CH_3CN reveal that the Mo(V/IV) couple in **1** is easier to reduce by 54 mV.

In pure acetonitrile, the pyranopterin form **1p** predominates at 86%, however, in the higher dielectric environment of 0.1 M tetrabutylammonium perchlorate (TBAP), the relative proportion of **1p** is likely well above 90%.[27] Probing the electrochemical behavior of **1** and **2** under variable scan rates (25–800 mV/s) in acetonitrile (Fig. S9) shows that $\Delta(E_c\text{-}E_a)$, the change in the peak-to-peak separation, is similar for both complexes and less than 20 mV, and i_c/i_a is near unity and varies from 0.98 – 1.05 over this scan rate range (Table S1) pointing to a simple reversible electrochemical process. This behavior is consistent with the interpretation that in ACN where the pyranopterin form **1p** is present >90%, the only event is the one electron redox at Mo. The cyclic voltammograms of **1** and **2** in chloroform, presented in Fig. S8, exhibit a smaller, 29 mV difference in the value of the Mo(V/IV)

potential that correlates with the smaller proportion (30%) of the pyranopterin form $\mathbf{1_p}$ in this solvent.

The difference in Mo(V/IV) potential between $\mathbf{1_p}$ and **2** is consistent with the Mo K-edge XANES data, which show that the rising edge of **1** is ~0.6 eV more positive than that of **2** (Fig. S7). The rising metal K-edge energy conveniently probes the effective nuclear charge on the metal ion and can be used to assign oxidation states.[31–33] In combination with ligand K-edge XAS data,[34–35] the electrochemical and Mo K-edge XANES allows for an assessment of ligand charge donation effects that control the charge on the metal ion, *vide infra*. Thus, the more positive Mo(V/IV) potential in the pyranopterin form of the ligand supports a hypothesis that the Mo ion in $\mathbf{1_p}$ is more electron deficient (e.g. more positively charged) than the Mo ion in **2**. This hypothesis is consistent from both a geometric and electronic structure perspective, since the greater π conjugation between the dithiolene and pterin groups in $\mathbf{1_p}$ facilitates S → pterin charge redistribution, leading to a concomitantly poorer S → Mo charge donation with the effect of stabilizing the electron rich Mo(IV) state.[36] Conversely, the more negative Mo(V/IV) reduction potential in **2** suggests a more electron rich Mo environment resulting from greater S → Mo charge donation.

Electronic Absorption Spectroscopy.

Room temperature solution electronic absorption spectra for **1** and **2** in DMSO are presented in Fig. 5. In DMSO, the pyrano form $\mathbf{1_p}$ predominates at approximately 93% over the open $\mathbf{1_o}$ form.[27] The observed differences in these two spectra provide a means by which we can better understand the implications of pyran ring opening on the electronic structure differences between these two complexes. Here, we observe that ring-closed $\mathbf{1_p}$ possesses two prominent charge transfer bands at ~22,500 cm^{-1} and 26,000 cm^{-1}. The electronic absorption band features for **2** are markedly less intense in this spectral region compared to $\mathbf{1_p}$, and they are also less well-defined. The complex and broadened spectrum observed for **2** likely arises from rotameric conformations about the dithiolenepterin C-C bond, with each rotamer contributing individually to the overall absorption envelope. The details of the electronic absorption spectra for **1** and **2** are discussed in greater detail below. The electronic absorption spectra of **1** and **2** in acetonitrile and chloroform are presented in Fig. S4 and S5. These spectra illustrate how solvent affects the electronic spectrum of **1** due to a change in the ratio of $\mathbf{1_p}$ to $\mathbf{1_o}$. This is most apparent on examining the spectrum of **1** in $CHCl_3$ which shows a markedly reduced absorptivity for the corresponding bands between 360–460 nm so that it more closely resembles the spectrum of **2** in chloroform. This is because in this low polarity solvent the open form $\mathbf{1_o}$ predominates ~70% over the cyclized, pyranopterin form $\mathbf{1_p}$.[27] This conclusion is supported by comparison of the extinction coefficients of these absorptions for **1** that are markedly larger in DMSO (386 nm, 15,980 M^{-1} cm^{-1}; 440 nm, 15,144 M^{-1} cm^{-1}) than in $CHCl_3$ (354 nm, 10,482 M^{-1} cm^{-1}; 448 nm, 7,036 M^{-1} cm^{-1}).

We have performed TDDFT calculations on $\mathbf{1_p}$ and **2** in order to make computationally assisted band assignments, and these assignments are summarized in Table S2. The Gaussian resolved absorption spectrum of $\mathbf{1_p}$ is given in Figure 6. Here, we observe that Band A (~20,000 cm^{-1}) is a low intensity band that is partially obscured by the low-energy tail of the more intense charge transfer (CT) absorption of Band B. The two one-electron promotions

that contribute to Band A intensity derive from a weak (HOMO) Mo(x^2-y^2) → LUMO (pterin) charge transfer and a (HOMO) Mo(x^2-y^2) → Mo(xz) ligand field (LF) excitation. The former is expected to dominantly contribute to the absorption intensity of this transition due to its charge transfer character. Pure LF transitions are expected in the 12,000 – 16,000 cm^{-1} range based on prior oxomolybdenum(V) spectra and are very weak in intensity. A detailed assignment of these LF transitions has been made for Tp*MoO(bdt) and Tp*MoO(tdt) based on their electronic absorption and MCD spectra. This study[11] also showed that the oscillator strengths of in-plane → out-of-plane CT transitions, similar to the HOMO Mo(x^2-y^2) → LUMO (pterin) transition in **1_p** (Table S2), are also expected to be weak with extinction coefficients ≲ 500 M^{-1}•cm^{-1}.[11] Band B is an intense CT band that can be assigned as a dithiolene → pterin ILCT transition. This transition principally derives from a symmetric dithiolene π HOMO-1 to pterin-based LUMO one-electron promotion. The intensity of Band C is predominantly due to LMCT character that results from a dithiolene-based HOMO-1 to Mo(xz) one electron promotion. Band D is the other intense CT feature that is observed prominently in the electronic absorption spectrum of **1_p**. Similar to Band B, this band is also assigned as a dithiolene → pterin ILCT transition. However, in contrast to Band B, this ILCT transition principally derives from a one-electron promotion that originates on the lower energy asymmetric dithiolene HOMO-2 orbital to the pterin LUMO. Compound **2** possesses decreased absorption intensity at energies lower than ~26,000 cm^{-1} when compared to **1_p**. This derives from the rotation of the oxidized pterin portion of the ligand out of the dithiolene plane (Fig. 3), which partially decouples the dithiolene and pterin. Tentative band assignments are based on the most stable rotameric conformer of **2**, identified through a DFT geometry optimization, where the pterin ring rotated ~40° out of the dithiolene plane (Fig. 3, right; Fig. S10–S11). All of the charge transfer transitions computed for **2** at energies less than ~ 25,000 cm^{-1} possess dominant dithiolene → pterin ILCT character. Electron density difference maps for the four lowest energy ILCT transitions computed for **2** are presented in Figure S6.

The pyran ring that connects the pterin and dithiolene groups in **1_p** enforces a nearly coplanar conformation of the pterin and dithiolene units, and this creates an extended conjugation from the Mo-dithiolene portion of the molecule out to the pterin (Fig. 8). The electron density difference map associated with the Band B transition is displayed in Fig. 7, and EDDMs associated with electronic excitations leading to Bands A, C, and D are displayed in Figure S12. The EDDM for the Band B ILCT clearly illustrates the loss of electron density from the dithiolene portion of the ligand (red), and the gain (green) to the pterin component of the ligand during the transition. We previously reported a similar ILCT transition in a related Mo complex that possesses a planar pyrrolo-quinoxaline-dithiolene ligand,[13, 16] and we anticipate that similar ILCT transitions will be observed for other dithiolene ligands that possess internal Donor-Acceptor (i.e. push-pull) character. Interestingly, a valence bond description (Fig. 8, top) of the aggregate dithiolene→pterin ILCT excited state character admixed into the electronic ground state of **1_p** is supported by the x-ray structure of this complex, *vide supra*, where the two Mo-S bonds are observed to be inequivalent (Fig. 8).

There are two important effects of the ILCT configurational mixing observed in **1_p**. The first is that the dithiolene→pterin charge transfer effectively reduces the donating ability of the dithiolene sulfurs.[13, 16, 37] This will stabilize the more electron rich reduced Mo(IV) state and destabilize the one-electron oxidized Mo(V) state, shifting the reduction potential to more positive values. The importance of dithiolene ligand donor ability has been highlighted by us previously, and we have shown how differences in dithiolene S → Mo charge donation across a series of Tp*MoO(dithiolene) complexes that possess different dithiolene ligands can modulate the Mo(V/IV) reduction potential by ~450 mV.[13, 16] Thus, the reduction in S → Mo charge donation for **1_p** is most likely the dominant contributor to the +54 mV Mo(V/IV) redox potential shift relative to **2**. The second effect of ILCT configurational mixing is that it effectively introduces oxidized thione-thiolate[13] valence bond character into the ground state wavefunction, which manifests itself in the aforementioned bond asymmetry within the dithiolene chelate ring. In summary, reduction in **π**-conjugation between the dithiolene and the pterin in **2** has the effect of decreasing S → pterin charge donation relative to **1_p**, contributing to a decrease in the Mo ion effective nuclear charge, and modifying the Mo(V/IV) reduction potential such that **2** is more difficult to reduce than **1_p** by 54 mV.

Infrared and Resonance Raman Spectroscopies.

FT-IR spectroscopy yields ν(Mo≡O) stretching frequencies of 924 cm^{-1} and 916 cm^{-1} for **1_p** and **2**, respectively. Previous studies have correlated ν(Mo≡O) stretching frequencies with the degree of S → Mo(xz,yz) charge donation,[38–40] with higher ν(MoO) frequencies correlating with a reduction in S → Mo(xz,yz) charge donation. Our results indicate less S → Mo(xz,yz) **π** donation in **1_p** as a consequence of sulfur electron density being delocalized onto the coplanar pterin acceptor component of the ligand. The loss of coplanarity between the pterin and dithiolene groups in **2** leads to a decrease in dithiolene-pterin **π**-conjugation and a corresponding increase in S → Mo(xz,yz) **π** donation that is reflected in the lower ν(Mo≡O) frequencies.

We have also collected solid-state resonance Raman (rR) data for **1_p** and **2** (Fig. 9). Pterin ring (C=C, C=N) and dithiolene ring (C=C) stretching contributions are anticipated in the 1450 – 1600 cm^{-1} region, and the dithiolene C=C stretch is expected in the 1500 – 1600 cm^{-1} region based on data for other oxo-molybdenum dithiolene systems.[41–44] Our computations indicate that additional C-C stretching and ring breathing contributions are expected in the 1340 – 1350 cm^{-1} region. Extensive mixing between characteristic high-frequency localized vibrations will result in a very complex normal mode description for **1_p** (see SI for resonance Raman based frequency assignments) Using a λ = 0.975 frequency scaling factor and making use of the computed resonance Raman intensities and frequencies for **1_p**, the two most enhanced vibrations observed on resonance with absorption band B are assigned as (1) a pterin-dithiolene stretching modes that possess dominant dithiolene C=C stretch and pterin (pyrazine) C=N stretch character (1508 cm^{-1}), and (2) a pterin-dithiolene mode with dominant dithiolene C=C stretch and pterin (pyrimidine) C=N stretch character (1549 cm^{-1}) (Fig. 10). We are also able to confidently assign the 1467 cm^{-1} vibration as a pterin ring mode with both C=N and C=C motions and the 1580 cm^{-1} vibration as a pterin mode with C=C stretching character. Similarly, our DFT frequency calculations for **2** allow

the 1505 cm^{-1} and 1553 cm^{-1} bands to be assigned to modes that possess dithiolene C=C and pterin C=N/C=C stretching character with mode descriptions that essentially parallel those for **1**. Resonance enhancement of the 1505 cm^{-1} and 1553 cm^{-1} bands, coupled with the similarity in appearance for the Raman spectra of **1** and **2**, indicates dithiolene → pterin charge transfer character is also present in the charge transfer bands of **2**.

S K-edge X-ray Absorption Spectroscopy.

S K-edge x-ray absorption spectroscopy is an indispensable method for proing the nature of metal-sulfur bonding and the degree of S character admixed into low-lying unoccupied or half-occupied molecular orbitals.[34, 44–50] Figure 11 displays the normalized S K-edge x-ray absorption spectra for compounds **1** and **2** in the solid state. Since the S 1s orbital is highly localized, electric dipole allowed transitions from this orbital occur to unoccupied valence molecular orbitals that possess S p orbital character (Figure 12). Thus, the relative intensities of the pre-edge features can be used to quantify the degree of S p-orbital character that is present in the virtual valence molecular orbitals of **1** and **2**.

Our bonding and TDDFT computations, charge transfer band assignments, and resonance Raman analysis all point to a LUMO wavefunction for **1** that is primarily pterin-dithiolene based with very little Mo d-orbital character. Thus, the lowest energy pre-edge transition (Band A) dominantly derives from S 1s → (pterin π^* + dithiolene S 3p) one-electron promotions. We note that for **2**, both of the low-energy pterin acceptor orbitals will contribute to the S pre-edge intensity of Band A through S 1s → (pterin π^* + dithiolene S 3p) one-electron promotions. The intensity of Band B derives from S 1s → (Mo 4d(xz,yz) + S 3p) one-electron promotions, which directly probe the degree of Mo-S bond covalency through S(p) → Mo(xz,yz) charge donation. We do not analyze the specific orbital contributions to Band C due the markedly higher density of states that contribute the S K-edge intensity at these higher energies. However, the computations indicate that the dominant S covalency contribution to Band C will derive from S 1s → Mo(x^2-y^2) one-electron promotions.

The procedure used to quantitate the amount of S p orbital character in the low-energy 1s → Ψ^* type transitions that comprise pre-edge Bands A and B is detailed in the SI. The total S character present in the pterin LUMO of **1** (2.2% total S) compared with the two pterin LUMOs of **2** (1.6% total S) shows that the S character in these pterin-based ILCT acceptor orbitals is small. In our analysis of Band B, we use $h = 4$ to obtain $\alpha^2 = 0.019$, or 1.9% S character per hole (3.8% total for the (xz,yz) pair) for the Mo(xz,yz) orbitals of **1**. This compares with 5.2% S character per hole (10.4% for the (xz,yz) pair) for the Mo(xz,yz) orbitals of **2**.

We have also analyzed this data in the context of TDDFT computations, which provide a good description of the experimental spectra (Fig. 13). The computational results support the lowest energy S 1s → S 3p transitions being to pterin-based orbitals, with the S 1s → (Mo 4d(xz,yz) + S 3p) transitions occurring at higher energy. The aggregate computed oscillator strengths that contribute to the intensity of Band 1 (**1**: f x10^{-4} = 7.3; **2**: f x10^{-4} = 7.8) show that the total S contribution to the pterin LUMO of **1** is nearly equal the that of the two

pterin acceptor orbitals in **2**. Similarly, the computed oscillator strengths for Band B (**1**: f x10^{-4} = 15.7; **2**: f x10^{-4} = 19.3) reflect a larger degree of Mo(xz,yz) – S(p) covalency in **2** compared to **1**. The analysis of the S K-edge data confirms the existence of low-lying pterin-based orbitals in **1** and **2** and supports our argument that the dithiolene sulfurs in **1** are poorer donors than those found in **2**. From a valence bond perspective, this can be described as resulting from a greater admixture of dithiolene → LUMO (pterin) ILCT character into the electronic ground state of **1**, leading to poorer S → Mo charge donation, an increase in the effective nuclear charge on Mo, and a positive shift in the reduction potential of **1** compared with **2**.

Discussion

Here we have presented a detailed study of two model Mo complexes where the pyranopterin-dithiolene in $\mathbf{1_p}$ is a close structural mimic of molybdopterin. Specifically, this study has explored the special ability of the pyranodihydropterin-dithiolene ligand to make small modulations in the Mo environment through second coordination effects. The results and analysis of the pyranopterin 'ring-closed' ($\mathbf{1_p}$) and 'ring-opened' (**2**) model systems provide data that are critical to understanding how changes in pterin-dithiolene conformation affect the electronic structure of the Mo active site in enzymes. This includes the underlying reasons why the pyranopterin plays such an essential role in molybdoenzyme catalysis, and how pyran cyclization dynamics in MPT could serve as molecular switch to fine-tune the Mo redox potential to further control catalytic activity in some molybdoenzymes.[20, 51–52] Analysis of spectroscopic and vibrational data for **1**, under conditions where $\mathbf{1_p}$ predominates, and **2** provide strong evidence for dithiolene S → pterin intraligand charge transfer character contributing to the ground state properties of these molecules and, by inference, to enzymes that have been hypothesized to employ semi-oxidized forms of the pterin analogous to $\mathbf{1_p}$ in their catalytic cycles.[24] Thus, the observation of strong ILCT transitions, as observed in $\mathbf{1_p}$, is diagnostic for the presence of a dihydropyranopterin structure. The Raman spectra obtained for $\mathbf{1_p}$ and **2** represent the first vibrational data for dihydropyranoterin dithiolene ligands that are complexed to an oxomolybdenum center. This is important, since the same dihydropyranopterin form of MPT, formally identified as the 10–10a dihydro form, has been hypothesized to be the form of MPT coordinated to the Mo ion in some molybdoenzymes.[24] We expect rR spectroscopy to be a powerful probe of MPT geometric and electronic structure in model systems and, where applicable, enzyme systems as well.[9–10] The S K-edge experiments reveal the intricate competition between S → Mo and S → pterin charge donations in $\mathbf{1_p}$ and **2**, which contributes to 1) increased thiol-thione resonance character being admixed into the ground state valence bond description of $\mathbf{1_p}$ relative to **2**, and 2) an observed +54 mV shift in the Mo(V/IV) reduction potential of $\mathbf{1_p}$ relative to **2** that stabilizes the reduced Mo(IV) state of $\mathbf{1_p}$.

This study was motivated by our curiosity about how variation in pterin structure, including changing redox state, might play a role in molybdenum enzymes. The nature of pterin-dithiolene electronic communication is important, since the MPT ligand has been postulated to function as an electron transfer conduit and a modulator of the enzyme reduction potential.[1–2, 9–11] Based on this study, it is clear that electronic coupling between the pterin

and dithiolene components of MPT will be enhanced for dihydropyranopterin structures such as **1_p** (Fig. 2) where the presence of a pyran ring enforces greater planarity between pterin and dithiolene components of the cofactor and facilitates π-conjugation in oxidized pyranopterins. In pyran ring-opened configurations, the electronic communication between the pterin and dithiolene components of the cofactor will be a function of the pterin-dithiolene interplane dihedral angle, with electronic communication being minimized when these planes are mutually orthogonal. Obviously, the protein environment will affect this dihedral angle to control **S** → pterin charge donation and the reduction potential. For the fully reduced tetrahydropterin form of the cofactor, the absence of a pterin π-system will result in dramatically less electronic communication with the dithiolene. Thus, the oxidation state of the pterin ring, coupled with the ring-opened/ring-closed nature of the pyran conspires to fine-tune the reduction potential of the Mo ion by modifying the electron donor ability of the dithiolene sulfurs. The results presented also provide new insight into the redox activation of specific molybdenum enzymes. There exist multiple reports[28–29, 53–55] of enzymes within the DMSOR family that are isolated as heterogeneous samples containing species that can be activated by a pre-reduction step. A recent investigation of one such enzyme, dissimilatory *E. coli* nitrate reductase (*Ec* Nar), studied the kinetics of the reductive activation using protein film voltammetry.[29] The kinetic analysis suggests that the inactive Nar enzyme involves two species in equilibrium where only one of these species is reducible. These researchers proposed that the equilibrium involves the cyclization of an open pterin in MPT to a pyranopterin form of MPT prior to a reduction step producing the active Nar enzyme, thereby ascribing a special role to the pyranopterin for accessing a necessary reduction step. The results we have obtained from models **1** and **2** provide the necessary data to confirm this hypothesis. Previously, we reported that the two forms of **1**, i.e., the open and pyranopterin forms shown in Fig. 2, exist in equilibrium with a K_{eq} value similar to that determined for the Nar enzymes.[29] Here, we have provided an electronic structure basis for understanding the differences in reduction potential between ring closed MPTs and their ring opened forms.

Summary

Molybdopterin, the unique pterin-dithiolene ligand present in all tungsten and non-nitrogenase molybdenum enzymes, is one of the most ancient ligands in bioinorganic chemistry, having been identified as present in the last universal common ancestor, LUCA.[6] Given its evolutionary importance and its ubiquity across phyla, it is astounding how little is known regarding its chemical behavior when bound to a metal within the protein. This dearth of information is due to the instability of Moco when removed from the protein host and the difficulty of probing its behavior *in situ* in the presence of other prosthetic groups.

Based on the results reported here, electronic coupling between pterin and dithiolene in the MPT ligand of Moco will be most favored for dihydropyranopterin structures analogous to **1_p** (Fig. 2) where the pyran maintains a planarity between the pterin and dithiolene to facilitate extended p-conjugation. In the absence of co-planar pterin and dithiolene, such as in **1_o** and **2** (Fig. 2), or in the absence of a pterin p-system such as in fully reduced tetrahydropterin, diminished electronic communication between pterin and dithiolene is expected since the π systems of the dithiolene and pterin units become decoupled. We show

that the coupled dihydropyranopterin-dithiolene unit can be identified by its signature strong intraligand charge transfer (ILCT) absorption. Furthermore, the admixture of the ILCT excited state configuration into the electronic ground state accentuates an electronic and geometric asymmetry in the dithiolene chelate, which may play an important role in directing electron flow through the pterin. These are the first quantitative studies that correlate a pterin structural change with measurable effects on the Mo electronic environment. The specific results from **1** and **2** provide a basis for understanding how the pyranopterin might play a role in molybdoenzyme catalysis by fine-tuning the Mo redox potential to control catalytic activity in some molybdoenzymes.

Materials and Methods

The syntheses of [TEA][Tp*Mo(S)(S_4)], 2-pivaloyl-6-chloropterin, and [TEA][Tp*Mo(O)(S_2BMOPP)], were performed using previously published procedures.[30] All other reagents, chemicals, and deuterated solvents were purchased from Sigma-Aldrich and used as received unless otherwise noted. All solvents for syntheses were purchased from Pharmco-AAPER and were deaerated with N_2 gas over activated neutral alumina before use. ESI-MS analyses were performed using a Waters Micromass-ZQ mass spectrometer via infusion of samples as acetonitrile solutions. All NMR experiments were performed on a Bruker 400 MHz FT-NMR. Infrared spectra were obtained using a PerkinElmer Frontier FT-IR on samples prepared as KBr pellets. Electronic absorption spectra were obtained using an Agilent 8453 spectrophotometer on samples in deaerated, anhydrous solvents. Electrochemical analysis was performed using a BASi Epsilon-EC potentiostat using 0.1 M tetrabutylammonium perchlorate (TBAP) as the electrolyte in anhydrous solvents, platinum working and auxiliary electrodes, and a Ag/AgCl reference electrode. All potentials were made in reference to an internal ferrocene potential (+440 mV in ACN and +510 mV in $CHCl_3$ vs. the Ag/AgCl electrode).

Synthesis of 6-(3-butynyl-2,2-dimethyl)-2-pivaloyl pterin (BDMPP)

2-pivaloyl-6-chloropterin (1.0074 g, 3.5842 mmol), CuI (0.1031 g, 0.5414 mmol), $Pd(OAc)_2$ (0.1009 g, 0.4494 mmol), and 1,1-bis(diphenylphosphino) ferrocene (DPPF) (0.2562 g, 0.4621 mmol) were combined in 30 mL acetonitrile and magnetically stirred for 10 minutes, after which 3,3-dimethyl-1-butyne (2.0 g, 25 mmol) and triethylamine (3.6 g, 35.9 mmol) were added via syringe under N_2 gas using standard Schlenk techniques. The resulting reddish-brown solution was stirred for 8 hours at room temperature, concentrated, and precipitated with diethyl ether (20 mL). Recrystallization of the residual solid from acetonitrile yields BDMPP (0.6834 g, 58.3%) as a cream solid. ^{1}H NMR ($CDCl_3$) δ: 12.35 (1H, bs, N-H), 8.80 (1H, s, pyrazine H), 8.35 (1H, bs, N-H), 1.35 (9H, s, -C(CH_3)$_3$), 1.34 (9H, s, -C(CH) −13 3). FT-IR (KBr pellet, cm^{-1}): ν(N–H) 3238, 3201, ν(C≡C) 2224, ν (C=O) 1682, 1620, ν (C=N) 1555, 1477, 1442. Anal. Calcd (%) for $C17.25H_{21.5}N_5O_2Cl_{0.5}$ (BDMPP ¼ CH_2Cl_2): C, 59.43; H, 6.22; N, 20.09. Found: C, 59.10; H, 6.14; N, 19.84.

Synthesis of [TEA][Tp*Mo^{4+}(S)(S_2BDMPP)] (3)

Under N_2 gas, [TEA][Tp*Mo(S)S_4] (0.2616 g, 0.3818 mmol) and BDMPP (0.1725 g, 0.5272 mmol) were magnetically stirred in acetonitrile (20 mL) to produce a brown solution that was heated for 53 hours at 45 °C. Vacuum concentration followed by addition of diethyl ether precipitated a plum brown solid that was subsequently filtered and dried under vacuum to yield **3** (0.3178 g, 87.8 %). FT-IR (KBr): ν(Mo≡S) 475. ESI^+MS: m/z: [M+2TEA]: 1078; ESI^-MS: m/z: [M]: 818.

Synthesis of [TEA][Tp*Mo^{4+}(O)(S_2BDMPP)] (2)

Under N_2 gas, a solution of **3** (0.3140 g, 0.3311 mmol) in acetonitrile (17 mL) was treated drop-wise with tributylphosphine (0.81 g, 4.0 mmol). The brown solution was stirred for two hours at room temperature, concentrated under vacuum, and precipitated by the addition of diethyl ether resulting in an oak brown solid that was filtered and dried under vacuum to produce **2** (0.2739 g, 88.7 %). ^{1}H NMR ($CDCl_3$) δ: 9.00 (1H, s, pyrazine H), 5.91 (1H, s, Tp* C-H), 5.84 (1H, s, Tp* C-H), 5.41 (1H, s, Tp* C-H), 4.64 (1H, bs, B-H), 2.75 (3H, s, $-CH_3$), 2.62 (3H, s, $-CH_3$), 2.40 (3H, s, $-CH_3$), 2.39 (3H, s, $-CH_3$), 2.24 (3H, s, $-CH_3$), 2.13 (3H, s, $-CH_3$), 1.35 (9H, s, $-C(CH_3)_3$), 1.27 (9H, s, $-C(CH_3)_3$). FT-IR (KBr): ν(Mo≡O) 916. ESI^+MS: m/z: [M+2TEA]: 1062; ESI^-MS: m/z: [M]: 802. UV/vis (CH_3CN), nm (ε, M^{-1} cm^{-1}): 289 (13,690), 337 (8,951). HRESI$^-$MS M = $C_{32}H_{43}O_3N_{11}BMoS_2$: m/z: [M-H as Mo^{5+}]: 801.20665. Calcd for M: m/z: 801.20661. Anal. Calcd (%) for $C_{40}H_{64}B_1N_{12}O_3S_2Mo_1$: C, 51.55; H, 6.922; N, 18.03. Found: C, 51.64; H, 7.22; N, 17.40.

Computational Methods

Ground state geometry optimization and energy calculations were performed at the density functional level of theory (DFT) using the Gaussian09 collection of software.[56] Input files were created and manipulated using Gaussview software. Calculations used the B3LYP hybrid functional. The Stuttgart/Dresden (SDD) basis set, and effective core potential, was applied to Mo, and the 6–31G* basis set was applied to all other atoms in the molecule. Pterin dihedral angle rotation calculations were performed starting with the optimized structure of **2**, and as the pterin dihedral angle was varied, the optimized structure for the remaining complex was maintained. Restricted time dependent DFT calculations were employed to produce the lowest-energy singlet and triplet excited states for the pyran form of **1** from its optimized singlet ground state geometry; assignment of the lowest energy (483 nm) transition was produced using GaussSum 2.2.5, and the electron density difference map (EDDM) was generated using GaussView. S K-edge XAS computations were conducted using ORCA (version 3.0.3) on the optimized geometry.[57] The def2-TZVP basis set, B3LYP functional, the zero-order regular approximation (ZORA) were used. The resonance Raman spectra were also computed in ORCA (4.0.0) at the density functional theory level using the B3LYP/G functional. The def2-TZVPP basis set was used for the Mo and S atoms, and def2-SVP was used for all light atoms. A numerical frequency calculation was performed on the optimized geometry to generate a Hessian file. This was followed by a TDDFT and an excited state gradient calculation, which were computed to generate an input file that is fed

into the advanced spectra analysis program (orce_asa). This program will predict the resonance enhancement of using a specific excitation wavelength.

Resonance Raman Spectroscopy

Samples for solid state resonance Raman spectroscopy were finely ground with a NaCl/Na_2SO_4 mixture (~10:1 by weight). These highly uniform samples were then flame sealed in quartz capillary tubes and placed in a spinning sample holder to minimize thermal and photochemical degradation. The Raman collection system utilizes a 90° scattering configuration. Samples were excited using Ar^+ (Coherent Innova 70) and Kr^+ (Coherent Innova 300) ion lasers (407 nm, 458 nm, 488 nm, 514 nm, 568 nm and 647 nm) with 50 mW of power at the sample. Laser plasma line contributions were removed using Semrock Maxline laser line filters, and the Rayleigh line contribution was reduced using Semrock Razor Edge long-pass filters. Raman scattered photons were focused onto the entrance slit of a PI/Acton Spectra SP-2500i 500 mm focal length spectrograph with a triple grating turret monochromator. The detection system employed a liquid-nitrogen cooled PI/Acton Spec-10:100B back illuminated 1340×100-pixel digit CCD camera detector. Raman shifts were calibrated against the 992 cm^{-1} band of the $Na_2SO_4^{2-}$ internal standard.

X-ray Absorption Spectroscopy

Mo K-edge X-ray absorption spectroscopic data were collected on beamline 7–3 at the Stanford Synchrotron Radiation Lightsource (SSRL) with the SPEAR storage ring containing 200 − 300 mA at 3.0 GeV. Beamline 7–3 is equipped with rhodium-coated mirrors upstream and downstream of the Si(220) double-crystal monochromator. The incident and transmitted X-ray intensities (I_0, I_1, and I_2) were monitored with three nitrogen-filled ionization chambers. The sample temperature was maintained at 10 K using an Oxford Instruments CF1208 continuous flow liquid helium cryostat. Samples were made using 4 mg of compound that was finely ground with 36 mg of BN powder. The samples were subsequently sealed in the sample holder using sulfur-free Kapton tape. Data were collected in florescence mode (Mo Ka) using a Lytle detector. A Zr-3 filter and a Soller slit were used before the detector to reject the scattered radiation. The internal energy was calibrated using a Mo foil reference with the first inflection point set to 20,000 eV. XAS data were processed using the Demeter software suite (version 0.9.25). The XANES spectra was calibrated and normalized in Athena with the threshold energy assigned as 20,010 eV. The data shown here are four-sweep averaged spectra. The EXAFS simulations were performed using Artemis. Backscattering paths were calculated from the embedded IFEFF (version IFEFF6) program using the DFT gas-phase optimized geometries for **1** and **2**. All Fourier transforms were phase corrected using Mo-oxo backscattering. The data-fitting range used is between 3 – 12 $Å^{-1}$ in k-space.

Sulfur K-edge XAS spectra were collected on beamline 4–3 at SSRL. BL4–3 is equipped with a liquid nitrogen cooled Si(111) double-crystal monochromator. The samples were prepared using a ground powder-on-tape protocol. The sample holder with powder-smeared-tape was placed in a helium-gas-purged sample chamber. All measurements were collected using the passivated implanted planar silicon (PIPS) fluorescence detector at room

temperature. The internal energy was calibrated to 2,472.02 eV using the $Na_2S_2O_3 \cdot 5H_2O$ as a calibrant. Data were plotted and processed to 2,510 eV due to the presence of Mo L3 edge peak (2,520 eV). The spectra reported here are averaged with four sweeps. The pre-edge features were fitted in Athena using one arctangent step line and several pseudo-Voigt peaks.

Supplementary Material

Refer to Web version on PubMed Central for supplementary material.

Acknowledgements

The authors acknowledge the National Institutes of Health (GM-057378 to M. L. K. and GM-081848 to S. J. N. B.) for continued financial support of our work on molybdoenzymes. S. J. N. B. also acknowledges the National Science Foundation (CHE-0958996). M. L. K. and J. Y. acknowledge SSRL staff members Erik Nelson and Matthew Latimer for their assistance and help with the collection of the XAS data. Use of the Stanford Synchrotron Radiation Lightsource and SLAC National Accelerator Laboratory is supported by the U.S. Department of Energy, Office of Science, Office of Basic Energy Sciences under Contract No. DE-AC02–76SF00515. M. L. K and J. Y. thank the UNM Center for Advanced Research Computing, supported in part by the National Science Foundation, for providing high performance computing resources used in this work. S. J. N. B. and D. G. thank Ben Rupert and Papa Nii Asare-Okai at the Mass Spectrometry Facility of the University of Delaware for HRESI analyses. D. G. and J. Y. equally contributed to this manuscript.

References

1. Kirk ML, Spectroscopic and Electronic Structure Studies of Mo Model Compounds and Enzymes In Molybdenum and Tungsten Enzymes: Spectroscopic and Theoretical Investigations, The Royal Society of Chemistry: Cambridge, UK, 2016.
2. Stein BW; Kirk ML, Electronic structure contributions to reactivity in xanthine oxidase family enzymes. Journal of Biological Inorganic Chemistry 2015, 20 (2), 183–194. [PubMed: 25425163]
3. Kirk ML; Stein B, The Molybdenum Enzymes In Comprehensive Inorganic Chemistry II (Second Edition), Editors-in-Chief: Jan R; Kenneth P, Eds. Elsevier: Amsterdam, 2013; pp 263–293.
4. Maia LB; Moura I; Moura JJG, Molybdenum and Tungsten-Containing Enzymes: An Overview. 2017; Vol. 5, p 1–80.
5. Hille R; Hall J; Basu P, The Mononuclear Molybdenum Enzymes. Chemical Reviews 2014, 114 (7), 3963–4038. [PubMed: 24467397]
6. Weiss MC; Sousa FL; Mrnjavac N; Neukirchen S; Roettger M; Nelson-Sathi S; Martin WF, The physiology and habitat of the last universal common ancestor. Nature Microbiology 2016, 1 (9).
7. Johnson J; Rajagopalan K, Structural and Metabolic Relationship Between the Molybdenum Cofactor and Urothione. Proc. Natl. Acad. Sci. U. S. A 1982, 79 (22), 6856–6860. [PubMed: 6960353]
8. Burgmayer SJN, Dithiolenes in Biology. John Wiley and Sons, Inc.: Hoboken, New Jersey, 2004; Vol. 52, p 491–538.
9. Dong C; Yang J; Reschke S; Leimkühler S; Kirk ML, Vibrational Probes of Molybdenum Cofactor–Protein Interactions in Xanthine Dehydrogenase. Inorg. Chem 2017, 56 (12), 6830–6837. [PubMed: 28590138]
10. Dong C; Yang J; Leimkühler S; Kirk ML, Pyranopterin Dithiolene Distortions Relevant to Electron Transfer in Xanthine Oxidase/Dehydrogenase. Inorg. Chem 2014, 53 (14), 7077–7079. [PubMed: 24979205]
11. Inscore FE; McNaughton R; Westcott BL; Helton ME; Jones R; Dhawan IK; Enemark JH; Kirk ML, Spectroscopic evidence for a unique bonding interaction in oxo-molybdenum dithiolate complexes: Implications for sigma electron transfer pathways in the pyranopterin dithiolate centers of enzymes. Inorg. Chem 1999, 38 (7), 1401–1410.

12. Jones RM; Inscore FE; Hille R; Kirk ML, Freeze-Quench Magnetic Circular Dichroism Spectroscopic Study of the “Very Rapid” Intermediate in Xanthine Oxidase. Inorg. Chem 1999, 38 (22), 4963–4970. [PubMed: 11671238]

13. Matz KG; Mtei RP; Rothstein R; Kirk ML; Burgmayer SJN, Study of Molybdenum(4+) Quinoxalyldithiolenes as Models for the Noninnocent Pyranopterin in the Molybdenum Cofactor. Inorg. Chem 2011, 50 (20), 9804–9815. [PubMed: 21894968]

14. Helton ME; Kirk ML, A model for ferricyanide-inhibited sulfite oxidase. Inorg. Chem 1999, 38 (20), 4384–4385. [PubMed: 11671145]

15. Inscore FE; Knottenbelt SZ; Rubie ND; Joshi HK; Kirk ML; Enemark JH, Understanding the origin of metal-sulfur vibrations in an oxo-molybdenurn dithiolene complex: Relevance to sulfite oxidase. Inorg. Chem 2006, 45 (3), 967. [PubMed: 16441102]

16. Matz KG; Mtei RP; Leung B; Burgmayer SJN; Kirk ML, Noninnocent Dithiolene Ligands: A New Oxomolybdenum Complex Possessing a Donor Acceptor Dithiolene Ligand. J. Am. Chem. Soc 2010, 132 (23), 7830–7831. [PubMed: 20481628]

17. Rothery RA; Stein B; Solomonson M; Kirk ML; Weiner JH, Pyranopterin conformation defines the function of molybdenum and tungsten enzymes. Proc. Natl. Acad. Sci. U. S. A 2012, 109 (37), 14773–14778. [PubMed: 22927383]

18. Rothery RA; Weiner JH, Shifting the metallocentric molybdoenzyme paradigm: the importance of pyranopterin coordination. Journal of Biological Inorganic Chemistry 2015, 20 (2), 349–372. [PubMed: 25267303]

19. Bertero MG; Rothery RA; Palak M; Hou C; Lim D; Blasco F; Weiner JH; Strynadka NCJ, Insights into the respiratory electron transfer pathway from the structure of nitrate reductase A. Nature Structural Biology 2003, 10 (9), 681–687. [PubMed: 12910261]

20. Kloer DP; Hagel C; Heider J; Schulz GE, Crystal structure of ethylbenzene dehydrogenase from Aromatoleum aromaticum. Structure 2006, 14 (9), 1377–1388. [PubMed: 16962969]

21. Youngblut MD; Tsai CL; Clark IC; Carlson HK; Maglaqui AP; Gau-Pan PS; Redford SA; Wong A; Tainer JA; Coates JD, Perchlorate Reductase Is Distinguished by Active Site Aromatic Gate Residues. J. Biol. Chem 2016, 291 (17), 9190–9202. [PubMed: 26940877]

22. Wu SY; Rothery RA; Weiner JH, Pyranopterin Coordination Controls Molybdenum Electrochemistry in Escherichia coli Nitrate Reductase. J. Biol. Chem 2015, 290 (41), 25164–25173. [PubMed: 26297003]

23. Duval S; Santini JM; Lemaire D; Chaspoul F; Russell MJ; Grimaldi S; Nitschke W; Schoepp-Cothenet B, The H-bond network surrounding the pyranopterins modulates redox cooperativity in the molybdenum-bisPGD cofactor in arsenite oxidase. Biochimica Et Biophysica Acta-Bioenergetics 2016, 1857 (9), 1353–1362.

24. Adamson H; Simonov AN; Kierzek M; Rothery RA; Weiner JH; Bond AM; Parkin A, Electrochemical evidence that pyranopterin redox chemistry controls the catalysis of YedY, a mononuclear Mo enzyme. Proc. Natl. Acad. Sci. U. S. A 2015, 112 (47), 14506–14511. [PubMed: 26561582]

25. Williams BR; Fu YC; Yap GPA; Burgmayer SJN, Structure and Reversible Pyran Formation in Molybdenum Pyranopterin Dithiolene Models of the Molybdenum Cofactor. J. Am. Chem. Soc 2012, 134 (48), 19584–19587. [PubMed: 23157708]

26. Abbreviations used: TEA = tetraethylammonium, Tp* = tris(3,5-dimethylpyrazolyl)hydroborate, BMOPP = 6-(3-butynyl-2-methyl-2-ol)-2-pivaloyl pterin BDMPP = 6-(3-butynyl-2,2-dimethyl)-2-pivaloyl pterin.

27. Williams BR; Gisewhite D; Kalinsky A; Esmail A; Burgmayer SJN, Solvent-Dependent Pyranopterin Cyclization in Molybdenum Cofactor Model Complexes. Inorg. Chem 2015, 54 (17), 8214–8222. [PubMed: 25942001]

28. Jacques JGJ; Fourmond V; Arnoux P; Sabaty M; Etienne E; Grosse S; Biaso F; Bertrand P; Pignol D; Leger C; Guigliarelli B; Burlat B, Reductive activation in periplasmic nitrate reductase involves chemical modifications of the Mo-cofactor beyond the first coordination sphere of the metal ion. Biochimica Et Biophysica Acta-Bioenergetics 2014, 1837 (2), 277–286.

29. Ceccaldi P; Rendon J; Leger C; Toci R; Guigliarelli B; Magalon A; Grimaldi S; Fourmond V, Reductive activation of E. coli respiratory nitrate reductase. Biochimica Et Biophysica Acta-Bioenergetics 2015, 1847 (10), 1055–1063.
30. Burgmayer SJN; Kim M; Petit R; Rothkopf A; Kim A; BelHamdounia S; Hou Y; Somogyi A; Habel-Rodriguez D; Williams A; Kirk ML, Synthesis, characterization, and spectroscopy of model molybdopterin complexes. J. Inorg. Biochem 2007, 101 (11–12), 1601–1616. [PubMed: 17765313]
31. Giles LJ; Ruppelt C; Yang J; Mendel RR; Bittner F; Kirk ML, Molybdenum Site Structure of MOSC Family Proteins. Inorg. Chem 2014, 53 (18), 9460–9462. [PubMed: 25166909]
32. Musgrave KB; Donahue JP; Lorber C; Holm RH; Hedman B; Hodgson KO, An X-ray spectroscopic investigation of bis(dithiolene)molybdenum(IV; V; VI) and -tungsten(IV; V; VI) complexes: Symmetrized structural representations of the active sites of molybdoenzymes in the DMSO reductase family and of tungstoenzymes in the AOR and F(M)DH families. J. Am. Chem. Soc 1999, 121 (44), 10297–10307.
33. George GN; Hilton J; Rajagopalan KV, X-Ray Absorption Spectroscopy of Dimethyl Sulfoxide Reductase from Rhodobacter sphaeroides. J. Am. Chem. Soc 1996, 118 (5), 1113–1117.
34. Sarangi R; George SD; Rudd DJ; Szilagyi RK; Ribas X; Rovira C; Almeida M; Hodgson KO; Hedman B; Solomon EI, Sulfur K-edge X-ray absorption spectroscopy as a probe of ligand-metal bond covalency: Metal vs ligand oxidation in copper and nickel dithiolene complexes. J. Am. Chem. Soc 2007, 129 (8), 2316–2326. [PubMed: 17269767]
35. Sproules S; Wieghardt K, Dithiolene radicals: Sulfur K-edge X-ray absorption spectroscopy and Harry's intuition. Coord. Chem. Rev 2011, 255 (7–8), 837–860.
36. Helton ME; Gruhn NE; McNaughton R; Kirk ML, Control of Oxo-Molybdenum Reduction and Ionization Potentials by Dithiolate Donors. Inorg. Chem 2000, 39 (11), 2273–2278. [PubMed: 12526484]
37. Mtei RP; Perera E; Mogesa B; Stein B; Basu P; Kirk ML, A Valence Bond Description of Dizwitterionic Dithiolene Character in an Oxomolybdenum-Bis(dithione) Complex. European Journal of Inorganic Chemistry 2011, (36), 5467–5470. [PubMed: 23956683]
38. Chang C-SJ; Enemark JH, Spectroscopic and Electrochemical Studies of Monomeric Oxomolybdenum(V) Complexes with Five-Membered Chelate Rings and Lakoxo or Alkanethiolato Ligands. Inorg. Chem 1991, 30, 683–688.
39. Garner CD; Hill L; Howlader NC; Hyde MR; Mabbs FE; Routledge VI, Crystal and Electronic-Structure and Reactivity of Mononuclear Halogeno-Oxomolybdenum(V) Complexes. Journal of the Less-Common Metals 1977, 54 (1), 27–34.
40. Subramanian P; Burgmayer S; Richards S; Szalai V; Spiro TG, Resonance Raman Signatures of Oxomolybdenum Thiolate and Dithiolene Models of Molybdenum Proteins. Inorg. Chem 1990, 29, 3849–3853.
41. Sugimoto H; Tatemoto S; Suyama K; Miyake H; Itoh S; Dong C; Yang J; Kirk ML, Dioxomolybdenum(VI) Complexes with Ene-1,2-dithiolate Ligands: Synthesis, Spectroscopy, and Oxygen Atom Transfer Reactivity. Inorg. Chem 2009, 48 (22), 10581–10590. [PubMed: 19831360]
42. Sugimoto H; Tatemoto S; Suyama K; Miyake H; Mtei RP; Itoh S; Kirk ML, Monooxomolybdenum(VI) Complexes Possessing Olefinic Dithiolene Ligands: Probing Mo-S Covalency Contributions to Electron Transfer in Dimethyl Sulfoxide Reductase Family Molybdoenzymes. Inorg. Chem 2010, 49 (12), 5368–5370. [PubMed: 20491454]
43. Sugimoto H; Tano H; Suyama K; Kobayashi T; Miyake H; Itoh S; Mtei RP; Kirk ML, Chalcogenidobis(ene-1,2-dithiolate)molybdenum(IV) complexes (chalcogenide E = O, S, Se): probing Mo≡E and ene-1,2-dithiolate substituent effects on geometric and electronic structure. Dalton Transactions 2011, 40, 1119–31. [PubMed: 21165484]
44. Tenderholt AL; Wang JJ; Szilagyi RK; Holm RH; Hodgson KO; Hedman B; Solomon EI, Sulfur K-Edge X-ray Absorption Spectroscopy and Density Functional Calculations on Mo(IV) and Mo(VI)=O Bis-dithiolenes: Insights into the Mechanism of Oxo Transfer in DMSO Reductase and Related Functional Analogues. J. Am. Chem. Soc 2010, 132 (24), 8359–8371. [PubMed: 20499905]

45. Szilagyi RK; Lim BS; Glaser T; Holm RH; Hedman B; Hodgson KO; Solomon EI, Description of the ground state wave functions of Ni dithiolenes using sulfur K-edge X-ray absorption spectroscopy. J. Am. Chem. Soc 2003, 125 (30), 9158–9169. [PubMed: 15369373]
46. Giles LJ; Grigoropoulos A; Szilagyi RK, Multi-edge X-ray absorption spectroscopy. 1. X-ray absorption near-edge structure analysis of a biomimetic model of FeFe-hydrogenase. The J. Phys. Chem.. A 2012, 116, 12280–98. [PubMed: 23145835]
47. Doonan CJ; Rubie ND; Peariso K; Harris HH; Knottenbelt SZ; George GN; Young CG; Kirk ML, Electronic structure description of the cis-MoOS unit in models for molybdenum hydroxylases. J. Am. Chem. Soc 2008, 130 (1), 55–65. [PubMed: 18062689]
48. Izumi Y; Glaser T; Rose K; McMaster J; Basu P; Enemark JH; Hedman B; Hodgson KO; Solomon EI, Ligand K-Edge and Metal L-Edge X-Ray Absorption Spectroscopy and Density Functional Calculations of Oxomolybdenum Complexes with Thiolate and Related Ligands: Implications for Sulfite Oxidase. J. Am. Chem. Soc 1999, 121 (43), 10035–10046.
49. Hatsui T; Takata Y; Kosugi N, Polarized Ni K- and L-edge and SK-edge XANES study of [Ni(III)(mnt)(2)](1-). Journal of Synchrotron Radiation 1999, 6 (pt.3)), 379–380. [PubMed: 15263314]
50. Peariso K; Helton ME; Duesler EN; Shadle SE; Kirk ML, Sulfur K-edge spectroscopic investigation of second coordination sphere effects in oxomolybdenum-thiolates: Relationship to molybdenum-cysteine covalency and electron transfer in sulfite oxidase. Inorg. Chem 2007, 46 (4), 1259–1267. [PubMed: 17291118]
51. Enemark JH; Garner CD, The Coordination Chemistry and Function of the Molybdenum Centres of the Oxomolybdoenzymes. J. Biol. Inorg. Chem 1997, 2 (6), 817–822.
52. Basu P; Burgmayer SJN, Pterin chemistry and its relationship to the molybdenum cofactor. Coord. Chem. Rev 2011, 255 (9,10), 1016–1038. [PubMed: 21607119]
53. Bray R; Adams B; Smith A; Bennett B; Bailey S, Reversible dissociation of thiolate ligands from molybdenum in an enzyme of the dimethyl sulfoxide reductase family. Biochemistry 2000, 39 (37), 11258–11269. [PubMed: 10985771]
54. Bell AF; He X; Ridge JP; Hanson GR; McEwan AG; Tonge PJ, Active site heterogeneity in dimethyl sulfoxide reductase from Rhodobacter capsulatus revealed by Raman spectroscopy. Biochemistry 2001, 40 (2), 440–448. [PubMed: 11148038]
55. George GN; Hilton J; Temple C; Prince RC; Rajagopalan KV, Structure of the Molybdenum Site of Dimethyl Sulfoxide Reductase. J. Am. Chem. Soc 1999, 121, 1256–1266.
56. Frisch MJ, W. T. G, Schlegel HB, Scuseria GE, Robb MA, Cheeseman JR, Scalmani G, Barone V, Mennucci B, Petersson GA, Nakatsuji H, Caricato M, Li X, Hratchian HP, Izmaylov AF, Bloino J, Zheng G, Sonnenberg JL, Hada M, Ehara M, Toyota K, Fukuda R, Hasegawa J, Ishida M, Nakajima T, Honda Y, Kitao O, Nakai H, Vreven T, Montgomery JA Jr., Peralta JE, Ogliaro F, Bearpark M, Heyd JJ, Brothers E, Kudin KN, Staroverov VN, Kobayashi R, Normand J, Raghavachari K, Rendell A, Burant JC, Iyengar SS, Tomasi J, Cossi M, Rega N, Millam JM, Klene M, Knox JE, Cross JB, Bakken V, Adamo C, Jaramillo J, Gomperts R, Stratmann RE, Yazyev O, Austin AJ, Cammi R, Pomelli C, Ochterski JW, Martin RL, Morokuma K, Zakrzewski VG, Voth GA, Salvador P, Dannenberg JJ, Dapprich S, Daniels AD, Farkas Ö, Foresman JB, Ortiz JV, Cioslowski J, and Fox DJ Gaussian 09, Gaussian, Inc.: Wallingford CT, 2009.
57. Neese F, The ORCA program system. Wiley Interdisciplinary Reviews: Computational Molecular Science 2012, 2 (1), 73–78.

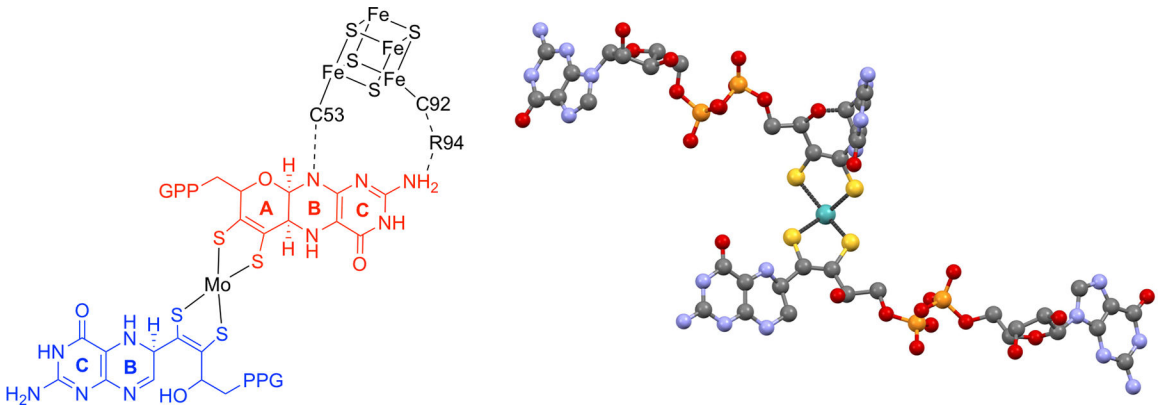

Figure 1.

(left) The two pterin dithiolene ligands of the periplasmic nitrate reductase NarGHI from *E. coli*. The pyranopterin dithiolene is comprised of pyrimidine (C), pyrazine (B), and pyran (A) rings of the proximal MPT (red) adjacent to the [4Fe-4S] cluster FS0, and the distal MPT (blue) is bicyclic.[7] Dashed lines represent hydrogen bonding interactions between Moco and FS0. A bidentate carboxylate interaction from Asp222 completes the Mo coordination sphere. PPG denotes a guanosine dinucleotide group. (right) Detailed view of Moco from NarGHI illustrating the markedly different conformations of the proximal vs distal pterin regions.

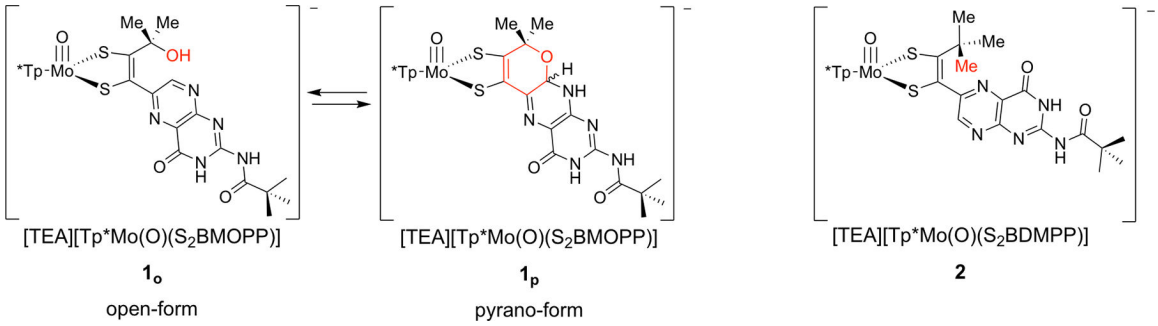

Figure 2.

(Left) Equilibrium of [TEA][Tp*Mo(O)(S_2BMOPP)] (**1**) between the open and pyran forms $\mathbf{1_o}$ and $\mathbf{1_p}$. (Right) [TEA][Tp*Mo(O)(S_2BDMPP)] (**2**) synthesized by isosteric replacement of a hydroxyl by a methyl group to preclude pyran ring formation.

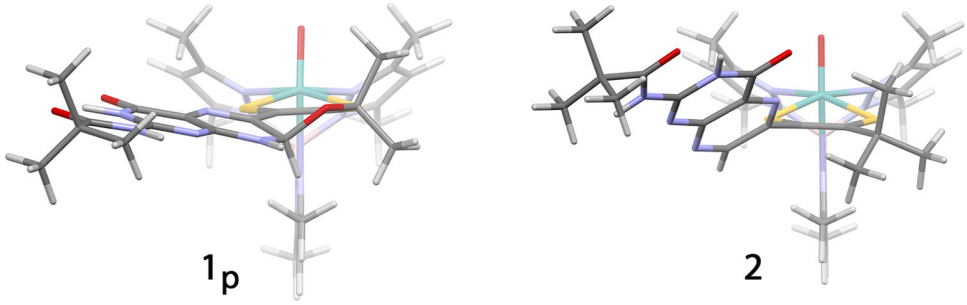

Figure 3.

(Left) X-ray structure of $\mathbf{1_p}$ shows that pyran formation enforces a nearly coplanar arrangement of the dithiolene and pterin systems, with the angle between the dithiolene chelate and the pterin rings 40° out of planarity being τ = 9°. (Right) The DFT optimized structure of **2** shows the pterin rotated $\tau \approx$ with the dithiolene due to a steric repulsion between the *t*-butyl group and the pterin.

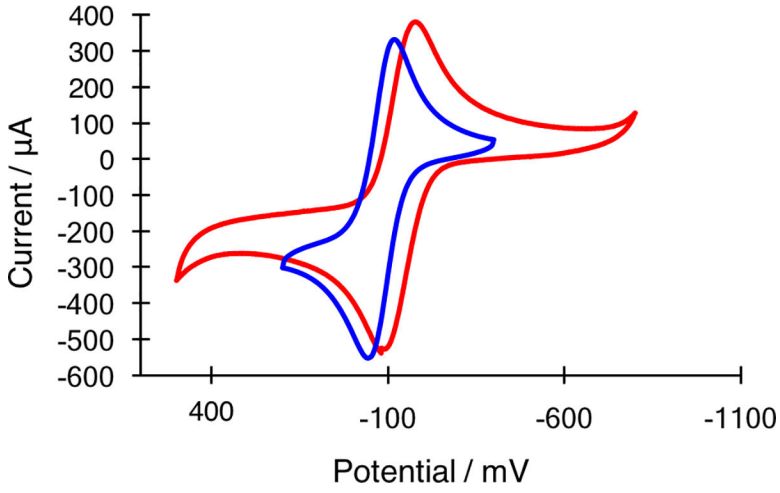

Figure 4.

Cyclic voltammograms of the Mo (V/IV) couple of **1** (blue) and **2** (red). The voltammograms are plotted versus the potential of reference electrode Ag/AgCl in (n-Bu_4N)(ClO_4)/CH_3CN at a scan rate of 100 mV/sec using a Pt working electrode. Mo(V/IV) potentials: **1** −520 mV, **2** −574 mV, vs Fc^+/Fc.

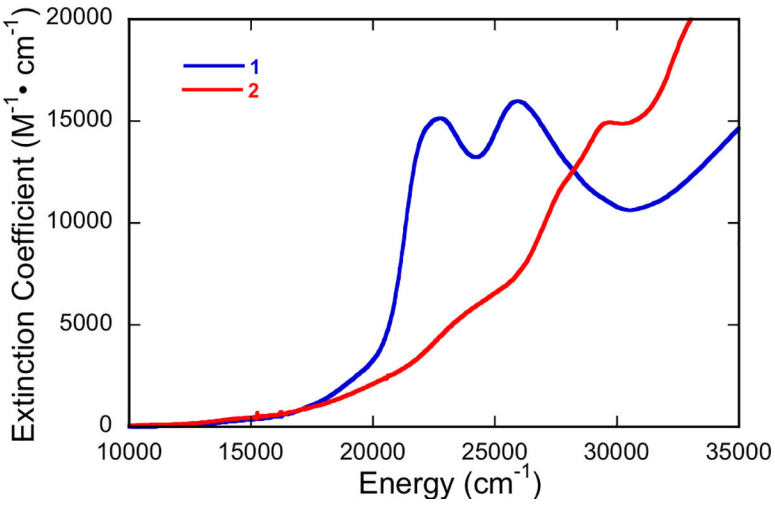

Figure 5.

Room temperature electronic absorption spectra of **1** (blue) and **2** (red), 3.00×10^{-5} M, in DMSO.

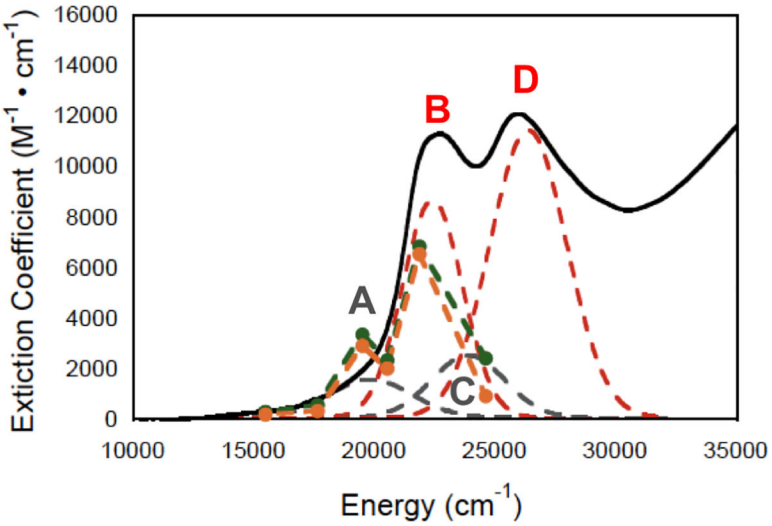

Figure 6.

Gaussian resolved electronic absorption spectrum of **1** in DMSO. Resonance Raman profiles for two high frequency S_2BMOPP ligand C=C stretches (green and orange dots) are included with Gaussian-resolved peaks corresponding to transitions A (grey), B (red), C (grey), and D (red). Resonance enhancement of these modes is fully consistent with our assignents of Bands A and B, which possess pterin LUMO acceptor character.

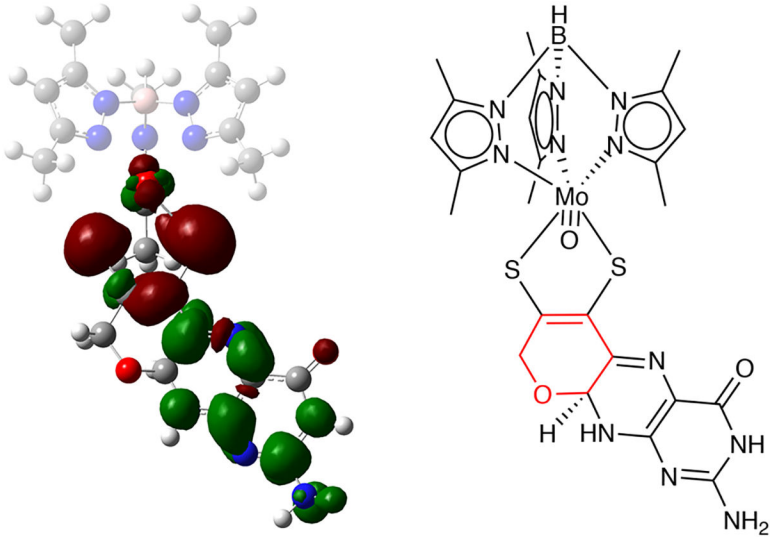

Figure 7.

Electron density difference map (EDDM; isovalue = 0.001) for Band B in **1** derived from TD-DFT pterin calculations showing dominant (74%) $S_{dithiolene} \rightarrow$ pterin character. Red regions represent a loss in electron density for the transition and green regions represent a gain in electron density for the transition. The molecule is oriented with the Mo≡O bond out of the plane and toward the reader. The bond line drawing illustrates the computational model, where the two methyl groups on pyran ring are replaced by protons and the pivaloyl group was removed from the amino group.

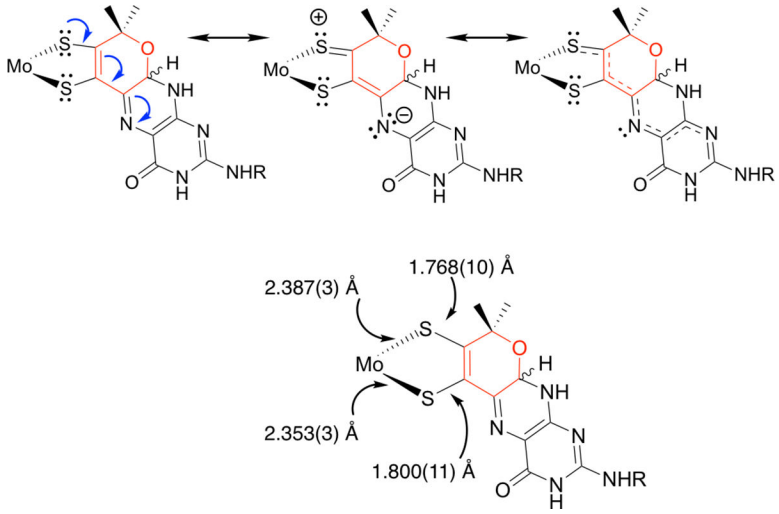

Figure 8.

(Top) Contributing resonance structures for **1**, with bond line drawing depicting the resultant extended π conjugation. (Bottom) Contributing resonance structures result from an admixture of ILCT excited states into the electronic ground state, and create bond asymmetry in the dithiolene chelate, which is observed in the bond metrics of the X-ray structure of **1**.25

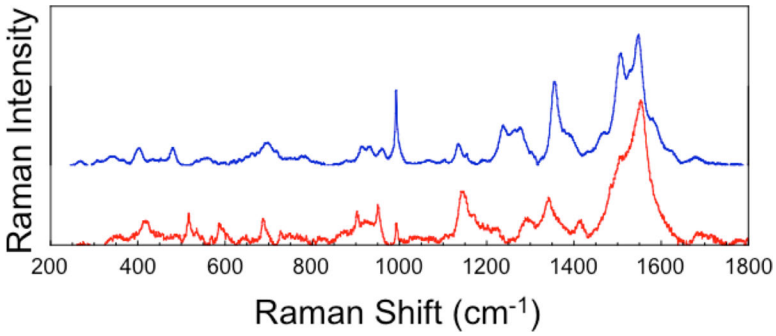

Figure 9.

Solid-state rR spectra (488 nm/20,492 cm^{-1} excitation) of **1** (blue) (50 mW) and **2** (red) (40 mW).

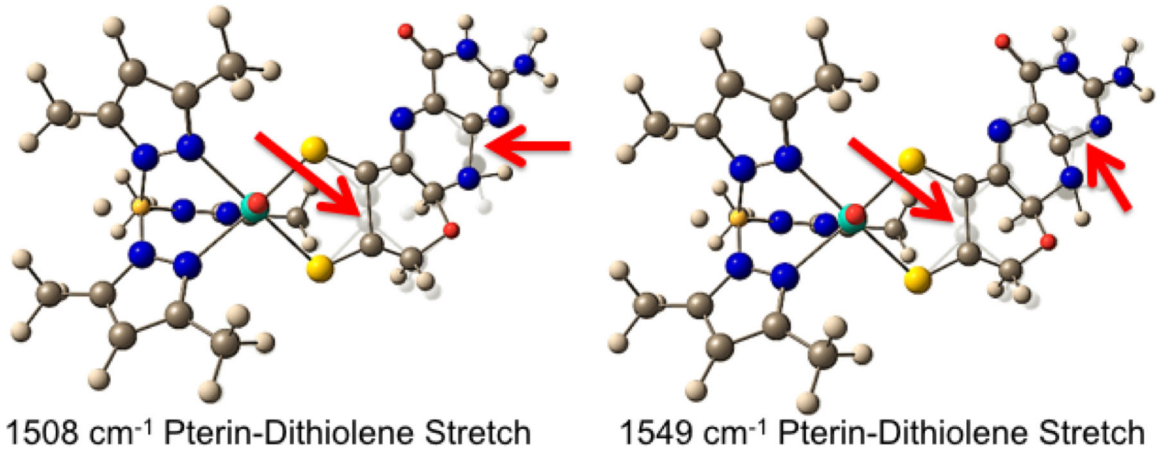

Figure 10.

DFT computed normal mode descriptions for the most resonantly enhanced pterin-dithiolene stretching vibrations in **1**.

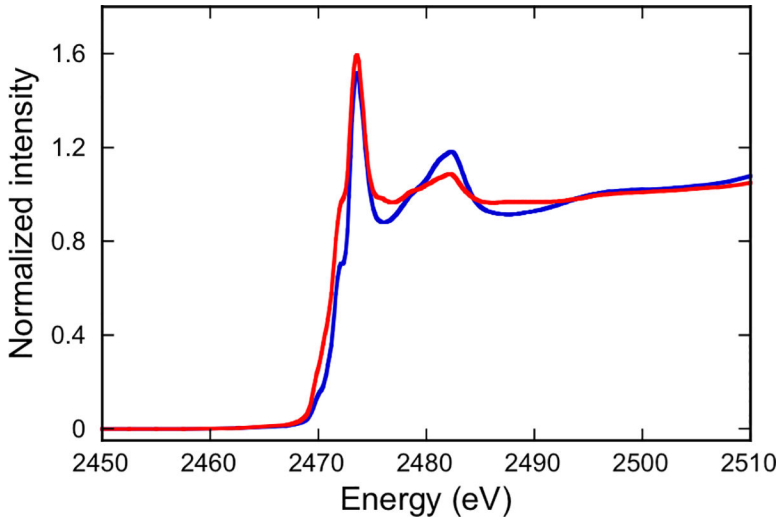

Figure 11.

S K-edge XAS spectra for **1** (blue) and **2** (red). The spectral range is limited to 2510 eV due to the presence of the Mo L3 absorption at 2520 eV. Note the greater pre-edge intensity of **2** relative to **1**, indicating a greater degree of S orbital character in the valence molecular orbitals of **2**.

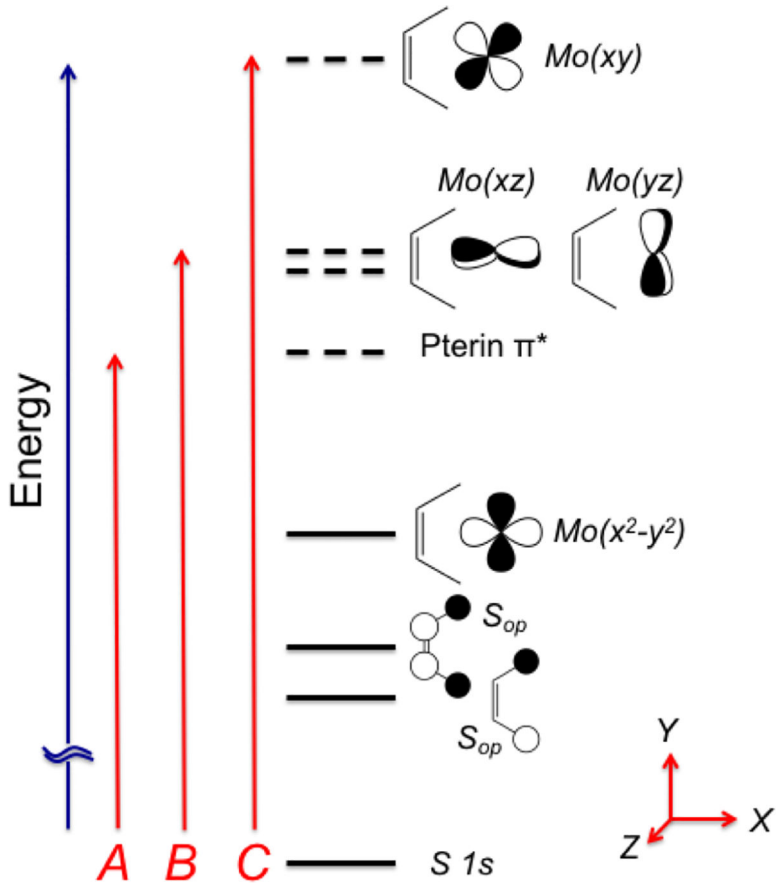

Figure 12.

Energy level diagram for S K-edge XAS analysis that is consistent with bonding calculations for **1** and **2**. Solid horizontal lines represent doubly occupied orbitals and dashed horizontal lines represent empty (virtual) orbitals. For **1**, the HOMO is the Mo(x^2-y^2) orbital and the LUMO is a pterin **π*** orbital. For **2**, there are two pterin **π*** orbitals. Higher energy acceptor orbitals for the S K-edge transitions are to the Mo(xz,yz) orbitals that are Mo≡O **π*** in nature, and the Mo(x^2-y^2) orbital which is **σ*** with the dithiolene S donors. Transitions A-C describe the nature of the S K-edge peaks observed in Figure 12. Note that the z-axis is orthogonal to the plane of the paper.

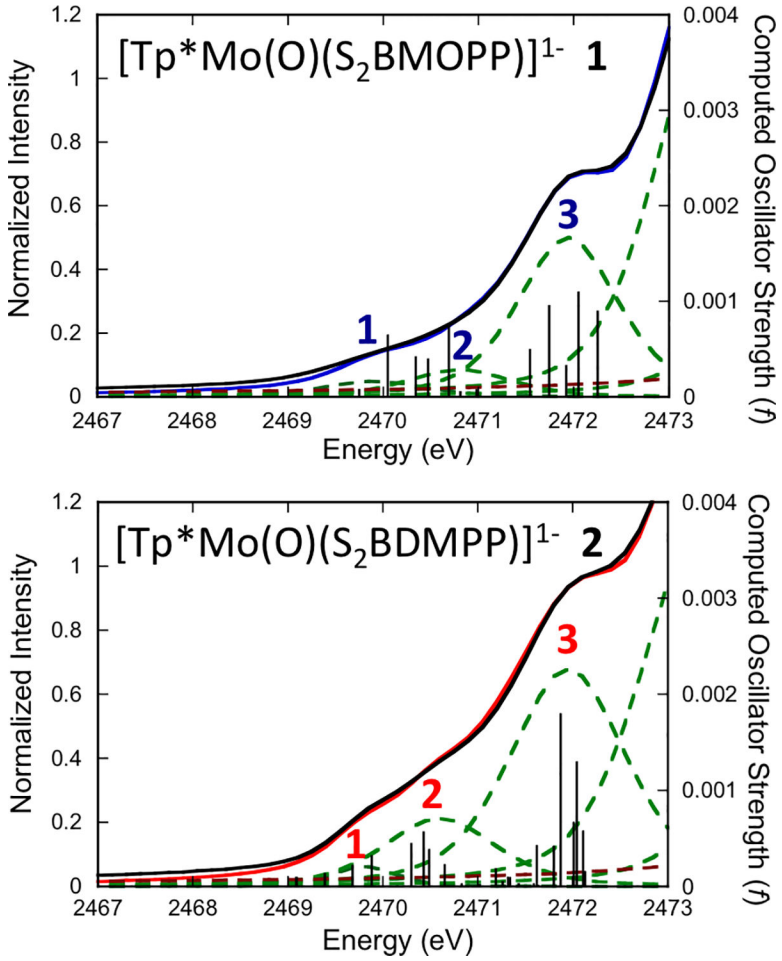

Figure 13.

Pseudo-Viogt fits (black) and individual fitted peaks (green) to the S K-edge pre-edge region for **1** (blue) and **2** (red). TDDFT computed transition energies and oscillator strengths for the individual S(1s) to valence orbital transitions are depicted as stick spectra for comparison. The TDDFT computed energies are shifted by +39.4 eV.

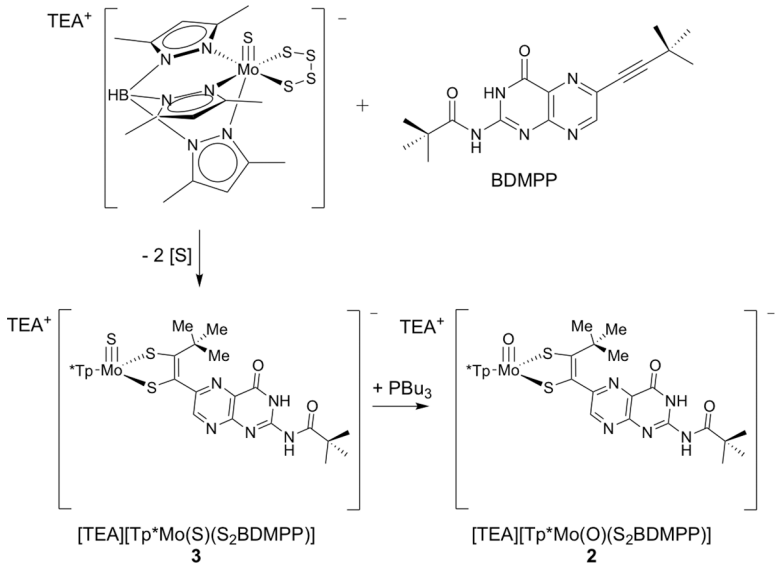

Scheme 1.

Synthetic route to [TEA][Tp*Mo(O)(S_2BDMPP)] **2**.